RESEARCH ARTICLE

ADVANCED
PHOTONICS
RESEARCH
Open Access

www.adpr-journal.com

Solar Degradation and Stability of Lead-Free Light Absorber Cs$_2$AgBiBr$_6$ in Ambient Conditions

Dennis Michael Jöckel, Songhak Yoon,* Alexander Frebel, Samuel Meles Neguse, Jürgen Dieter Rossa, Alexander Jürgen Bett, Martin Schubert, Marc Widenmeyer, Benjamin Balke–Grünewald, and Anke Weidenkaff

As numerous studies on highly efficient perovskite solar cells have been conducted on lead-based light absorbers, such as MAPbI$_3$ and FAPbI$_3$, increasing concerns are rising regarding toxicity and stability issues. One of the most prominent and promising lead-free alternatives is the double-perovskite Cs$_2$AgBiBr$_6$, which is well-suited for multi-junction solar cells considering its relatively large indirect bandgap of around 1.95–2.05 eV. Despite distinctive reports on its performance under ambient conditions, the demonstrated stability has not yet been conclusively clarified. Within this study, the degradation behavior of Cs$_2$AgBiBr$_6$ single crystals is investigated under different ambient environments, such as AM1.5g solar irradiation, aquatic conditions, and humidity. The corresponding samples are analyzed by using Raman, UV–vis, energy-dispersive X-Ray, and micro-photoluminescence spectroscopies together with X-Ray diffraction. High intrinsic stability of Cs$_2$AgBiBr$_6$ in ambient conditions and severe degradation in aquatic conditions are observed. Furthermore, surface morphology alterations are found during the simulated solar irradiation indicating photo-accelerated degradation behavior. In the results of this study, it is clearly implied that intense research efforts need to be put into sealing the Cs$_2$AgBiBr$_6$ layer in solar cells with the goal of protecting it from humidity and water intrusion simultaneously, therefore avoiding photo-accelerated degradation.

1. Introduction

Single-junction perovskite solar cells (PSCs) have lately been achieving increasingly high power conversion efficiencies (PCEs) up to 26.1% near the Shockley–Queisser limit.[1] However, many of the most competitive solar cells are based on the toxic element lead (Pb), e.g., MAPbI$_3$ and FAPbI$_3$ employing methylammonium (MA$^+$) and formamidinium (FA$^+$),[2] which is the reason for the recent trend to consider lead-free alternatives for PSCs, such as the double-perovskite Cs$_2$AgBiBr$_6$. With a reported bandgap of 1.95–2.05 eV,[3–5] Cs$_2$AgBiBr$_6$ is likely to be employed in upper layers of multi-junction solar cells.[6,7] Despite efforts to decrease its bandgap resulting, for example, in a reported PCE of 6.37% for hydrogenated Cs$_2$AgBiBr$_6$,[8] most research on Cs$_2$AgBiBr$_6$ solar cell devices focuses on improving their charge-carrier mobility and lifetime.[9–12] Numerical simulation studies showed a theoretical PCE of up to 7.25% can be achieved in multi-junction PSCs at an optimal Cs$_2$AgBiBr$_6$ layer thickness of 600 nm.[10,12] However, concerns about the long-term stability of Cs$_2$AgBiBr$_6$ have been reported.[13–17] The scientific literature agrees upon a thermal stability of up to 250 °C.[3,4,16,18–20] Regarding the material's stability in ambient conditions, some research groups have reported high stability,[16,18,21–23] while others observed instability toward air and humidity.[3,20] Opinions diverge further when considering the photostability of Cs$_2$AgBiBr$_6$. As with general ambient stability, some report no alteration during exposure to light,[17,21,24] while others see a clear trend toward photodegradation behavior.[4,14,20] For instance, Dakshinamurthy and Sudakar[14] investigated the photostability of Cs$_2$AgBiBr$_6$ and found heavy degradation resulted from induced heating by the utilization of a high-power laser. Thus, there is a significant scientific uncertainty and a knowledge gap regarding the ambient and photostability of Cs$_2$AgBiBr$_6$ in relevant ambient conditions. The goal of this study is to further investigate the behavior of Cs$_2$AgBiBr$_6$ in different ambient environments and to clarify relevant degradation mechanisms. Circularity and ecological sustainability, two key aspects for ensuring a secure future, ought to be considered for every newly investigated material. Hence, a regenerative

D. M. Jöckel, S. Yoon, A. Frebel, S. M. Neguse, J. D. Rossa,
B. Balke–Grünewald, A. Weidenkaff
Fraunhofer Research Institution for Materials Recycling and Resource Strategies IWKS
Aschaffenburger Straße 121, Hanau 63457, Germany
E-mail: song.hak.yoon@iwks.fraunhofer.de

A. ü. Bett, M. Schubert
Fraunhofer Institute for Solar Energy Systems ISE
Heidenhofstraße 2, Freiburg 79110, Germany

M. Widenmeyer, A. Weidenkaff
Department of Materials and Earth Sciences
Technical University of Darmstadt
Peter–Grünberg–Straße 2, Darmstadt 64287, Germany

ⓘD The ORCID identification number(s) for the author(s) of this article can be found under https://doi.org/10.1002/adpr.202300269.

synthesis from reused HBr solvent was conducted within this study to assess the material's potential for a sustainable industrial-scale production.

2. Experimental Section

2.1. Synthesis

Four $Cs_2AgBiBr_6$ samples (A–D) exposed to distinctive environments (as depicted in **Table 1**) and three references (R1: as synthesized $Cs_2AgBiBr_6$, R2: sealed dark reference $Cs_2AgBiBr_6$, and R3: $Cs_3Bi_2Br_9$) were investigated within the scope of this study. The precursors including CsBr (99.9%, metal basis, Alfa Aesar), AgBr (99.5%, Alfa Aesar), and $BiBr_3$ (99%, Alfa Aesar) were used as received (see Equation (1)). All samples were mixed in a stoichiometric ratio of 2:1:1 in 20 mL 0.07 M aqueous HBr solution (48%, Alfa Aesar). All $Cs_2AgBiBr_6$ samples were synthesized via solution cooling method from 80 °C to room temperature at a cooling rate of $3\,K\,h^{-1}$ ($5\,K\,h^{-1}$ for regenerative sample RS and reference R4) on a hot plate according to the synthesis route described by Yin et al.[25]

$$2CsBr + AgBr + BiBr_3 + HBr\,(aq.)$$
$$\rightarrow Cs_2AgBiBr_6 + HBr\,(aq.) \tag{1}$$
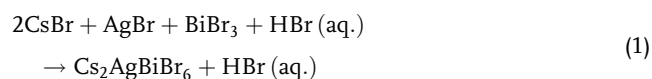
A comparably quick cooling rate was chosen to obtain small crystals with diameters below 1 mm to avoid grinding for spectroscopy measurements. The synthesized crystals were instantly separated by decanting the solution. The $Cs_3Bi_2Br_9$ reference sample (R3) was grown via hydrothermal synthesis in a microwave digestion system (Turbowave 1500, MLS). The synthesis condition was the same as that reported in our previous work.[26]

2.2. Simulated Environments

Four different ambient environments were simulated to investigate the behavior of $Cs_2AgBiBr_6$ single crystals and the resulting deviation in optical properties and degradation mechanisms. Two samples were put in the dark, out of which one was left open to laboratory conditions (A: Dark_dry) at a relative humidity of 20%–50%. And, 2 mL of water was added to $Cs_2AgBiBr_6$ single crystals for direct contact (C: Dark_wet), which was also exposed to open laboratory conditions. Two other samples were irradiated for 140 h with a near AM1.5g spectrum (420–1050 nm) simulated with a VeraSol solar simulator by Oriel Instruments.

Both samples were left open under laboratory conditions. One was left dry (B: Rad_dry) and to the other 2 mL of water was added (D: Rad_wet). All samples were exposed to their respective aforementioned environments for 140 h at room temperature. Afterward, all samples were sealed under ambient conditions at the same time and consequently stored in the dark before further characterization. A detailed chemical analysis of the used water is given in Table S1, Supporting Information. In addition, three references R1 (original $Cs_2AgBiBr_6$ sample measured before simulation runs), R2 (sealed dark reference measured after simulation runs), and R3 ($Cs_3Bi_2Br_9$ single crystals obtained via hydrothermal synthesis) were investigated. The goal was to better understand the intrinsic stability of the single crystals as well as the effect of the secondary phases. Detailed information about simulated environment setups and reference samples are listed in Table 1.

Furthermore, the three precursors CsBr, AgBr, and $BiBr_3$ used for synthesis were also analyzed via Raman spectroscopy (see Figure S3, Supporting Information). In addition to the simulated environment setups, the first successful regenerative synthesis of $Cs_2AgBiBr_6$ with preused HBr solvent was conducted to investigate its potential with regard to recyclability and scalability. For this purpose, the remaining precursor concentration was approximated by reintroducing the same precursor mass as originally recovered by the anterior synthesis (shown in **Table 2**).

2.3. Characterization Methods

UV-vis spectroscopy was conducted with a Perkin Elmer Lambda 900 spectroscope in the range of 200–800 nm. By using the Kubelka–Munk function $F(R)$, the absorbance a was approximated from the measured reflectance R of each sample according to Kubelka and Munk (Equation (2)).[27]

$$a \approx F(R) = \frac{(1-R)^2}{2R} \tag{2}$$

To estimate, the indirect bandgaps of each sample Tauc plots, as described by Makuła et al.[28] were utilized. Calculation of the indirect bandgap was based on Equation (3)

$$(a\,h\nu)^{\frac{1}{2}} = B(h\nu - E_g) \tag{3}$$

where h is the Planck constant, ν is the photon frequency, E_g is the bandgap, and B is a constant. For further analysis of the lattice vibration modes, Raman spectroscopy was conducted with a

Table 1. Simulated environment setups and reference samples.

Sample	Air and humidity	Water	Light	Time of exposure
A: Dark_dry	Open (RH = 20%–50%)	Humidity	None	140 h
B: Rad_dry	Open (RH = 20%–50%)	Humidity	AM1.5g	140 h
C: Dark_wet	Open (RH = 20%–50%)	2 mL water	None	140 h
D: Rad_wet	Open (RH = 20%–50%)	2 mL water	AM1.5g	140 h
R1: $Cs_2AgBiBr_6$ before simulations	Closed	None	None	None
R2: $Cs_2AgBiBr_6$ after simulations	Closed	None	None	None
R3: $Cs_3Bi_2Br_9$ reference	Closed	None	None	None

Table 2. Synthesis of recycled sample (RS) and normal synthesis reference (R4).

Sample	CsBr [g]	AgBr [g]	BiBr$_3$ [g]	HBr [mL]	Precursor concentration [M]	Cooling rate [K h^{-1}]
RS: Regenerative sample	0.0681	0.0300	0.0722	8.4 (reused)	<0.07	5
R4: Fresh HBr reference	0.2501	0.1105	0.2640	8.4 (fresh)	0.07	5

Bruker Senterra spectroscope. An excitation wavelength of 632.8 nm (He–Ne laser) was applied with a resolution of 2–5 cm^{-1} in a measured range of 55–250 cm^{-1}. An objective lens with a magnification of 20 and an aperture of 25 μm was chosen. The measurements were repeated 10 times for each sample, and the obtained spectra were averaged. For surface morphology and compositional analysis, a Zeiss Merlin field-emission scanning electron microscope (SEM) coupled with energy-dispersive X–ray spectroscopy (EDX) was employed with an acceleration voltage of 15 kV. Powder X-ray diffraction (XRD) patterns were obtained using a Malvern PANalytical Empyrean diffractometer (Co-K$\alpha_{1,2}$ radiation) to identify the phases present in the samples. The diffraction patterns were recorded in a 2θ range of 10°–100° with an angular step interval of 0.013°.

Samples B and R2 were further examined via micro-photoluminescence (micro-PL) spectroscopy. The PL measurements were carried out using a confocal microscope. The frequency-doubled neodymium-doped yttrium aluminum garnet solid-state laser (wavelength of 532 nm and intensity of ≈10 μW) was focused onto the sample using an objective lens (50× magnification, numerical aperture = 0.65). The luminescence of a small area (2 μm in diameter) was investigated. The reflected laser light was hindered from reaching the pinhole (diameter 100 μm) by a beam splitter and a long pass filter. The PL signal was directed onto a grating spectrometer (600 g mm^{-1}) and detected using a silicon charge-coupled device. To account for spectrally different collection efficiencies of the detection unit, a calibration lamp with known spectrum I_{CL} was measured. The PL signal was calculated from the raw data S_{meas} and the measured calibration lamp spectrum S_{CL} using the relation depicted in Equation (4).

$$PL = \frac{\frac{(S_{meas} - O_1)}{t_1}}{\frac{(S_{CL} - O_2)}{t_2}} \cdot I_{CL} \qquad (4)$$

with $t_1 = 0.1$ s and $t_2 = 0.05$ s being the integration times used for the measured PL and calibration lamp, respectively; O_1 and O_2 are the corresponding offset spectra (dark spectra). A Gaussian fit was performed to the obtained calibrated spectra for the estimation of the peak position and intensity of the spectra.
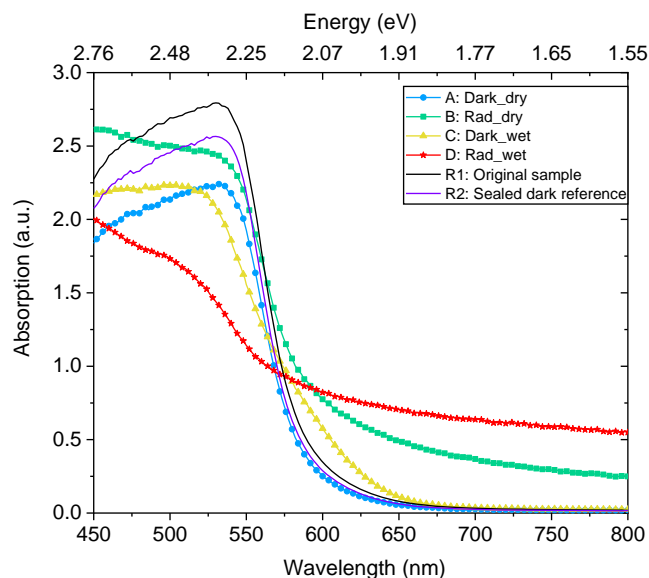
3. Results

3.1. Optical Microscopy and SEM

The samples exposed to aquatic conditions (C: Dark_wet and D: Rad_wet) exhibited clear signs of degradation visible to the naked eye. Investigations with the optical microscope (**Figure 1**a) and the SEM (Figure 1b) confirmed high degrees of degradation of the wet samples. Multiple distinctive structural changes (crystalline and amorphous phases) and different colors including red, yellow, orange, and even white could be observed, which were absent in the references R1 and R2 (Figure S1, Supporting Information). Both radiated Sample B: Rad_dry and Sample D: Rad_wet depicted a surface darkening compared to the dark Sample A: Dark_dry and Sample C: Dark_wet. Furthermore, Sample B depicted irregularities in the size of 0.5–μm (Figure 1a,b). The morphology changes on Sample B were further investigated with EDX and micro-PL.

3.2. UV–Vis Spectroscopy and Bandgap Determination

The UV–vis absorption spectra of all samples with the references R1 and R2 are displayed in **Figure 2**. All tested samples (A–D) lost absorption intensity at the typical local absorption maximum at 2.34 eV (≈530 nm) compared to the original sample R1. Although their measurements were offset by 62 d, R2 obtained a very similar absorption curve compared to R1 with corresponding bandgaps of 2.05 eV (R1) and 2.04 eV (R2) (compared to
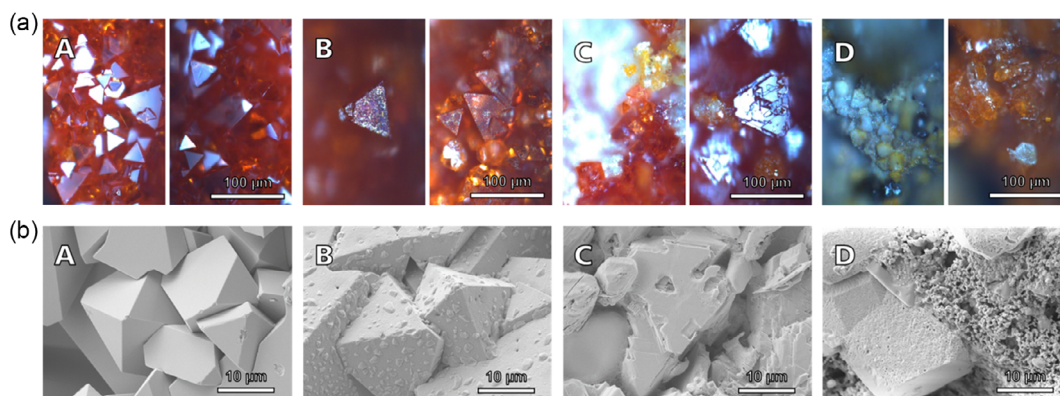
Figure 1. a) Optical microscope images (two different locations on each sample) and b) scanning electron microscope images for Samples A, B, C, and D.

**ADVANCED
SCIENCE NEWS**

www.advancedsciencenews.com

**ADVANCED
PHOTONICS
RESEARCH**
Open Access

www.adpr-journal.com

Figure 2. UV-vis absorption spectra of the Samples A, B, C, and D, and the references R1 (original sample) and R2 (sealed dark reference).

Table 3. Comparison of indirect bandgap and Raman A_{1g} FWHM of the $Cs_2AgBiBr_6$ samples.

Sample	Indirect bandgap [eV]	Raman A_{1g} FWHM [cm^{-1}]
A: Dark_dry	2.04	11.48
B: Rad_dry	2.04	12.26
C: Dark_wet	1.87	12.59
D: Rad_wet	2.10	18.03
R1: Original sample	2.05	11.41
R2: Sealed dark reference	2.04	11.24

Table 3). The highest decrease in peak absorption and the highest absorbance increase below the typical bandgap could be observed for Sample D: Rad_wet. Interestingly, Sample B: Rad_dry also showed a significant increase in the absorption intensities compared to reference samples at longer wavelengths. The spectra over the whole measurement range can be found in Figure S2, Supporting Information. Regarding the estimated bandgaps, there was no significant bandgap deviation for all dry Samples A, B, and R2 compared to R1. However, Sample C: Dark_wet exhibited a substantial bandgap decrease toward 1.87 eV, while Sample D: Rad_wet demonstrated a bandgap deviation toward 2.10 eV.

3.3. Raman Spectroscopy

For both wet Samples C and D, new intensity maxima were observed in Raman spectroscopy as shown in **Figure 3**. Typical $Cs_2AgBiBr_6$ spectra without additional bands were observed within the measured range for A, B, and R1. For a comparison, the precursors CsBr, AgBr, and BiBr$_3$ used for synthesis and two abnormal spectra of Sample D are shown in Figure S3, Supporting Information. All four samples (A–D) exhibited local
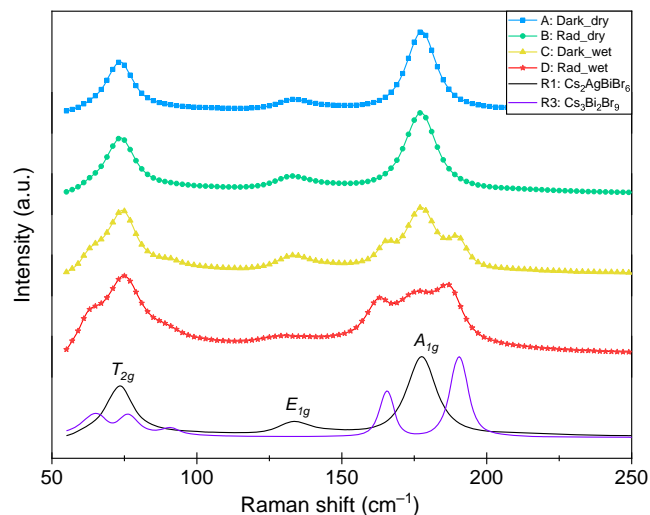
Figure 3. Raman spectra of Samples A, B, C, and D, and the references R1 and R3 normalized to the respective global maximum.

maxima at the typical Raman bands T_{2g} (73.5–75.0 cm^{-1}), E_g (131.0–133.5 cm^{-1}), and A_{1g} (177.0–177.5 cm^{-1}) in good accordance with previous reports.[14,19,29] However, for Sample C: Dark_wet and Sample D: Rad_wet additional bands corresponding to $Cs_3Bi_2Br_9$ were observed. Sample D was the only one not showing a global maximum at the typical A_{1g} band as an indication for high amounts of secondary phases. The concentration of lattice defects or degree of imperfections as additional signs for degradation was further examined by estimating the full widths at half maxima (FWHM) of the A_{1g} band and is displayed in Table 3. Sample D: Rad_wet revealed the highest FWHM value, followed by Sample C: Dark_wet and Sample B: Rad_dry. Even though their measurements were offset by 62 d, no significant change in FWHM was observable for R2 and Sample A compared to the original Sample R1. R2 even achieved the overall lowest FWHM despite the storage time.

3.4. Micro-PL Spectroscopy

The impact of solar irradiation on a dry $Cs_2AgBiBr_6$ surface was further investigated by micro-PL spectroscopy. In **Figure 4**, the Sample B: Rad_dry and Sample R2: Sealed dark reference are depicted via SEM (Figure 4a,d) and the respective measurement locations are shown on optical microscopy images (Figure 4b,e). The PL peak positions obtained from spatially resolved micro-PL measurements are depicted in Figure 4c,f. Reference R2 exhibited a spatially homogeneous PL peak position as shown in Figure 4c, while PL peak positions with many irregularities are observed on Sample B (Figure 4f).

3.5. SEM-EDX Spectroscopy

The averaged atomic contents determined by EDX spectroscopy are listed in **Table 4**. Only the elements O, Cs, Ag, Bi, and Br were considered in the analysis yielding averaged trends in ratios among these elements. Furthermore, Samples B and D exhibited similarities in elemental compositions averaged by five different
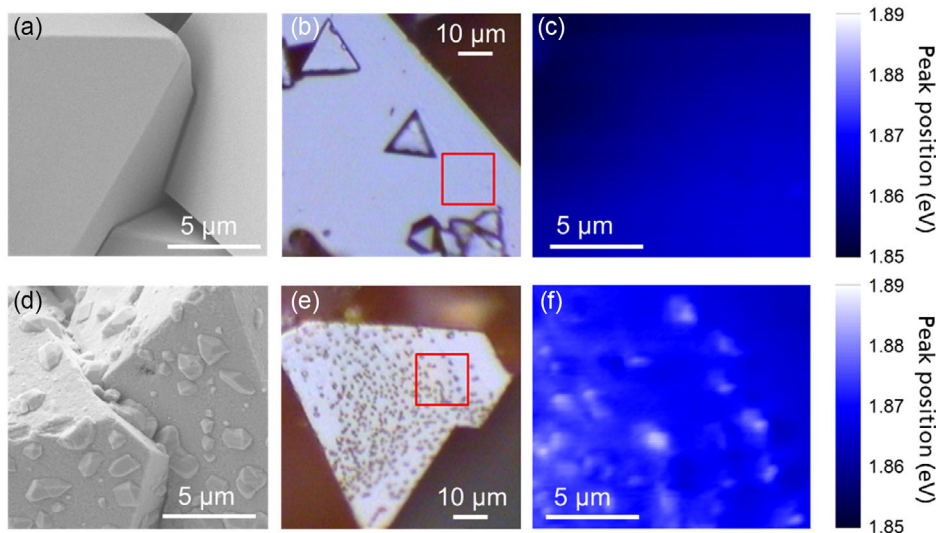
Figure 4. Surface of reference R2 compared to Sample B captured via a,d) SEM, b,e) optical microscopy, and c,f) micro-PL mapping. The PL measurement area is shown as a red rectangle on the optical microscope images in b) for reference R2 with corresponding PL peak positional mapping in c). The same applies to Sample B e) with corresponding PL peak positional mapping f).

Table 4. Averaged atomic contents (at%) for samples a, B, C, D, and R2.

Sample	O [at%]	Cs [at%]	Ag [at%]	Bi [at%]	Br [at%]
A: Dark_dry	3.2	19.9	10.7	9.5	56.7
B: Rad_dry	13.3	17.0	13.6	9.0	47.0
C: Dark_wet	5.9	24.7	10.5	6.4	52.5
D: Rad_wet	14.5	17.1	13.9	9.3	45.2
R2: Sealed dark reference	2.3	23.4	10.9	9.2	54.2

measurements for each sample, with the highest Ag and O contents and the lowest Cs and Br contents among all samples. For all samples, Bi and Br contents were found to be below the expected atomic share of 10 and 60 at%, respectively. Ag generally was observed to be more abundant near the surfaces (>10 at. %), especially in the radiated Sample B: Rad_dry and Sample D: Dark_wet. Investigating the average crystal composition indirectly indicated the possible presence of secondary phases such as $Cs_3Bi_2Br_9$, $CsAgBr_2$, and $CsBr$. The detailed EDX spectra and corresponding measurement locations are shown in Figure S4, Supporting Information.

3.6. Powder XRD

The powder XRD patterns (Figure S5, Supporting Information) of four samples (A–D) exhibited distinctive changes after exposure to by simulated environments. Both Sample A: Dark_dry and Sample B: Rad_dry showed no detectable secondary phases indicating that the concentrations of potential secondary phases are under the detection limit. However, as shown in Figure S5b, Supporting Information, the presence of secondary phases $CsAgBr_2$, $BiBrO$, and $Cs_3Bi_2Br_9$[30–32] was identified for Sample C: Dark_wet and Sample D: Rad_wet.

3.7. Regenerative Synthesis

Regenerative synthesis was conducted by reusing the solution after the first synthesis. A total relative yield of 35.6 wt% could be achieved for the regenerative sample RS with the same synthesis method. However, significantly, a smaller precursor amount was used for the regenerative sample RS compared to the fresh reference R4 (see **Table 5**). The obtained FWHM value for Raman A_{1g} band of RS was comparable to those of reference Samples R1, R2, and R4. Despite the similar indirect bandgap, its absorption behavior was inferior to that of R4, displaying absorption below the bandgap and an overall lower typical absorption maximum above the bandgap (**Figure 5**a). Minor impurities and a darker color could be observed for sample RS compared to R4. Nonetheless, Raman spectroscopy confirmed that no secondary phases could be identified in either sample (Figure 5b,c).
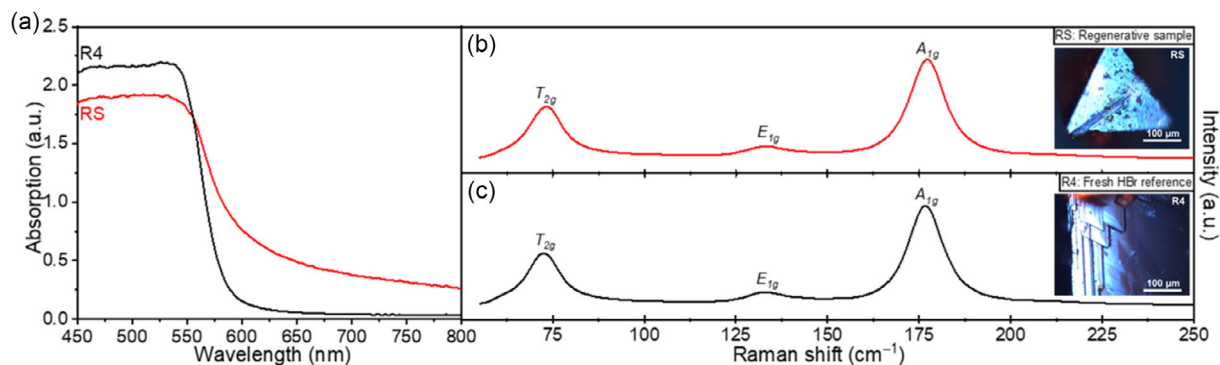
4. Discussion

4.1. Ambient Stability Overtime

As 2 months passed between the measurements of R1 and R2, the excellent state of R2 clearly indicates strong time stability (compare R1 and R2 in Figure 4 and Table 3). Also, good ambient stability was observed for $Cs_2AgBiBr_6$ single crystals left open to air in relative humidity of 20%–50% for 140 h (R1 and R2

Table 5. Total precursor mass, yield, indirect bandgaps, and Raman FWHM broadening of recycled synthesis RS and fresh HBr reference R4.

Sample	Precursor mass [g]	Crystal yield [g]	Relative yield	Bandgap [eV]	A_{1g} FWHM [cm^{-1}]
RS: Regenerative sample	0.170	0.061	35.6 %	2.06	11.25
R4: Fresh reference	0.625	0.221	35.4 %	2.08	11.14

**ADVANCED
SCIENCE NEWS**

www.advancedsciencenews.com

**ADVANCED
PHOTONICS
RESEARCH**
Open Access

www.adpr-journal.com

Figure 5. a) UV–vis absorption spectra of R4 and RS, b) Raman spectroscopy for regenerative sample RS, and c) Raman spectroscopy for reference R4.

compared to A: Dark_dry in Figure 3 and 4; Table 3 and 4). Furthermore, the A_{1g} FWHM broadening of R2 even decreased from 11.41 cm^{-1} (R1) to 11.24 cm^{-1} (R2) after being stored in the dark for 2 months (Table 3). This observation could be explained by the fact that HBr solvent remained after the synthesis, which likely had an influence on the highly surface-sensitive Raman signal of R1. In the case of R2, there was more time for HBr evaporation. In addition, despite having been exposed to air at 20%–50% relative humidity, Sample A: Dark_dry showed a very similar A_{1g} FWHM broadening and bandgap values compared to those of the original reference R1 (Table 3).

4.2. Moisture and Water Instability

Moisture-induced degradation of $Cs_2AgBiBr_6$ could be confirmed with SEM and optical microscopy. The formation of multiple secondary phases with different colors, shapes, and structures in both wet Samples C and D was indicated (compare Figure 1). As shown in **Figure 6**a, the resulting multi-phase structure of Sample C was more crystalline than that of Sample D (Figure 6b) and exhibited more of the original $Cs_2AgBiBr_6$ crystal shape. By using Raman spectroscopy, the secondary-phase $Cs_3Bi_2Br_9$ could be identified in both Samples C and D (Figure 3, S2, and S3, Supporting Information). The resulting Raman spectra were similar to those reported by Pistor et al.[19] for a $Cs_2AgBiBr_6$ sample heated to 275 °C. Figure 6c indicates the presence of hexagonal-shaped $Cs_3Bi_2Br_9$ crystals in good agreement with previous findings on $Cs_3Bi_2Br_9$.[31,33] Furthermore, an amorphous structure with the elemental

composition of the CsBr precursor (Figure S2 and S3b, Supporting Information) and its typical white color were observed (Figure 1a). The XRD patterns shown in Figure S5, Supporting Information, confirmed the formation of secondary phases observed by Raman spectroscopy. In addition to $Cs_3Bi_2Br_9$, the phases $CsAgBr_2$ and BiBrO could be identified by XRD (Figure S5, Supporting Information). $CsAgBr_2$ was also confirmed by EDX spectroscopy (Figure S2 and S3c, Supporting Information). The indirect bandgaps of both wet samples showed an opposing trend with a decrease to 1.87 eV (Sample C: Dark_wet) and an increase to 2.10 eV (Sample D: Rad_wet, compare Table 3). For Sample D, this hints toward defects and an influence of the abundant secondary-phase $Cs_3Bi_2Br_9$ with its higher reported bandgap.[31,33] It should be also noted that no clear relation between the averaged atomic surface composition of both wet Samples C and D was found when comparing the EDX results (Table 4). Overall, the wet samples displayed clear moisture-induced degradation. Especially, the combination of moisture and simulated sunlight results in an apparent change of chemical composition and have a significant influence on the morphology of the remaining $Cs_2AgBiBr_6$ bulk phase.

4.3. Photostability

In the past years, debatable statements have been made regarding the photostability of $Cs_2AgBiBr_6$, including good stability in extreme conditions[18] and no degradation under constant illumination (e.g., under N_2 atmosphere),[16,17,22] laser-induced (thermal) degradation,[14] discolorations after illumination,[4]
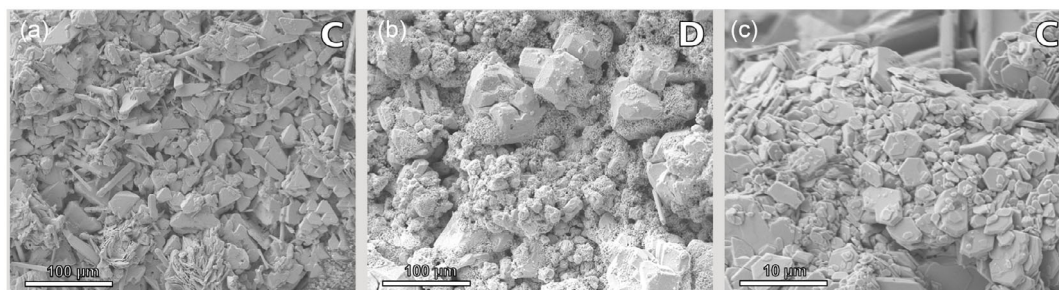
Figure 6. SEM photos of a) Sample C (Dark_wet), b) Sample D (Rad_wet), and c) hexagonal secondary phases on the surface of Sample C indicating the presence of $Cs_3Bi_2Br_9$.

**ADVANCED
SCIENCE NEWS**

www.advancedsciencenews.com
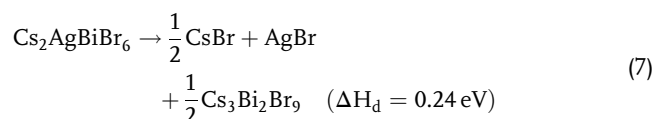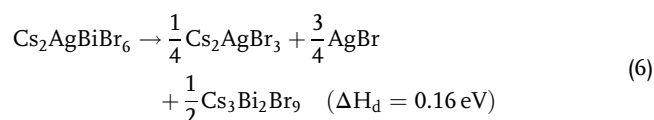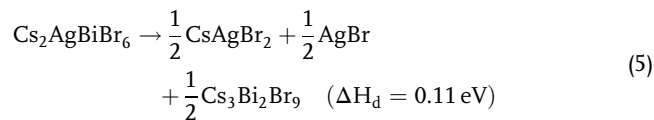
**ADVANCED
PHOTONICS
RESEARCH**

www.adpr-journal.com

and secondary-phase formations after light exposure.[34] One of the findings in this study was the darkening of both illuminated samples (B: Rad_dry and D: Rad_wet) compared to their counterparts (A: Dark_dry and C: Dark_wet) as can be seen in Figure 1a. Possible reasons for that were the visible roughness and the irregularities on the surfaces of Samples B and D (Figure 1b). As shown in Figure 2, the UV–vis absorption spectra of both radiated Samples B and D revealed increased background absorbance at longer wavelengths. As no secondary phases were detected in Sample B by Raman spectroscopy or XRD, this was likely to originate from the generation of lattice defects or surface irregularities. In Samples C and D, in contrast, secondary phases including $Cs_3Bi_2Br_9$, $CsAgBr_2$, and $BiBrO$ were identified. Only Sample D showed higher absorbance than Sample B. Therefore, it is most likely that surface irregularities and defects dominantly affect the absorption behavior at longer wavelengths in this study. Regarding the contribution of $Cs_3Bi_2Br_9$ as the dominant secondary phase formed during water-induced degradation, $Cs_3Bi_2Br_9$ has been reported to have a direct bandgap of 2.64–2.71 eV, revealing the higher bandgap compared to $Cs_2AgBiBr_6$.[30,35] Hence, for severely degraded wet Samples C and D, the absorbance at shorter wavelengths possibly was affected by the presence of $Cs_3Bi_2Br_9$.

In both SEM and PL mapping images, irregularities in the size of 0.5–3 μm were observed on the surface of Sample B: Rad_dry, which is comparable to the size of big water droplets in humid environments and could therefore have resulted from humidity.[36] However, pure humidity-induced degradation could be excluded due to the absence of irregularities on the surface of the open Sample A: Dark_dry (Figure 1a,b), which was exposed to the same humidity. A similar finding of light-induced surface discolorations in $Cs_2AgBiBr_6$ was reported by Slavney et al. after irradiation under an N_2 atmosphere.[4] Hence, it can be concluded that discolorations can clearly be explained with photoinduced degradation. When investigating both irradiated samples with EDX spectroscopy, there was a clear trend regarding the averaged atomic surface contents of both irradiated Samples B and D. Both obtained significantly increased oxygen content (13.3 and 14.5 at%), a high share of Ag (13.6 and 13.9 at%), and lower Br (47.0 and 45.2 at%), and Cs (17.0 and 17.1 at%) contents. The Bi content did only marginally deviate from that of reference R2 or Sample A. The increase in atomic Ag content could be a hint for the previously discussed Ag–Bi ion migration in $Cs_2AgBiBr_6$.[13,37] The insignificant change in surface Bi and the simultaneous vanishing of Cs and Br and increase of Ag and O determined by EDX could imply, for instance, locally silver-rich defective $Cs_2AgBiBr_6$ phases forming on the surface induced by the AM1.5g illumination. This would consequently leave behind a $Cs_2AgBiBr_6$ bulk structure with Ag vacancies, which could explain the likely presence of defects (or segregates) indicated by the high absorption intensities of Samples B and D between 600 and 800 nm in UV–vis absorption spectra (Figure 2 and S2, Supporting Information).

4.4. Thermodynamic Degradation Pathways

When investigating the theoretic thermodynamic nature of $Cs_2AgBiBr_6$, it is crucial to consider its decomposition pathways. Xiao et al. reported three energetically most plausible reactions[37]

$$Cs_2AgBiBr_6 \rightarrow \frac{1}{2}CsAgBr_2 + \frac{1}{2}AgBr$$
$$+ \frac{1}{2}Cs_3Bi_2Br_9 \quad (\Delta H_d = 0.11\,eV) \quad (5)$$

$$Cs_2AgBiBr_6 \rightarrow \frac{1}{4}Cs_2AgBr_3 + \frac{3}{4}AgBr$$
$$+ \frac{1}{2}Cs_3Bi_2Br_9 \quad (\Delta H_d = 0.16\,eV) \quad (6)$$

$$Cs_2AgBiBr_6 \rightarrow \frac{1}{2}CsBr + AgBr$$
$$+ \frac{1}{2}Cs_3Bi_2Br_9 \quad (\Delta H_d = 0.24\,eV) \quad (7)$$

Including the more energy-intensive degradation into the original precursor chemicals

$$Cs_2AgBiBr_6 \rightarrow 2CsBr + AgBr + BiBr_3 \quad (\Delta H_d = 0.64\,eV) \quad (8)$$
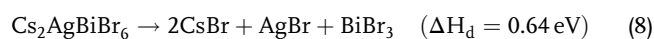
The three main pathways include $Cs_3Bi_2Br_9$ as a product. Its presence in the wet Samples C and D was indicated by yellow colors in optical microscopy (Figure 1a), hexagonal crystal shapes in SEM (Figure 6c), and EDX composition (Table S2 and Figure S4b, Supporting Information). It was confirmed for both wet Samples C and D via Raman spectroscopy (Figure 3) and powder XRD (Figure S5, Supporting Information). Additionally, XRD clearly indicated the presence of identified $CsAgBr_2$ in both wet Samples C and D, proving that (Equation (5)) is the most likely decomposition pathway. Even though a compositional analysis by using EDX needs to be carefully considered, the determined stoichiometric composition of $CsAgBr_2$ (compare Table S2 and Figure S4a, Supporting Information) was also noticeable. However, it should be mentioned that the overlap effect of other secondary phases such as CsBr and AgBr cannot be excluded. Furthermore, BiBrO was identified by XRD analysis in both wet samples hinting toward surface oxidation in the presence of water and air.

As depicted in **Figure 7**, the irradiated samples have a significantly higher surface content of silver and oxygen, while the highest Cs content was obtained for Sample C. Secondary phases like AgBr, BiBrO, and $CsAgBr_2$ on $Cs_2AgBiBr_6$ have also been reported in the literature.[21,34,38,39] $CsAgBr_2$ was found by Makani et al. and their EDX results (atomic ratio of 26:25:49 [Cs:Ag:Br]) are comparable to the ratio of 29.6:25.5:49 (Cs:Ag:Br) obtained from Sample C (compare Figure S4a and Table S2, Supporting Information). The high Cs amount in combination with high oxygen content could also hint toward the presence of cesium oxides or cesium hydroxide on the surface.[38] Cesium hydroxide is a strong base,[40,41] so its presence would pose a significant risk to PSC's performance. Consequently, its formation on $Cs_2AgBiBr_6$ surfaces and device interfaces should be avoided at any cost. For Sample B, no secondary phases were not detected by Raman spectroscopy. Nonetheless, EDX point measurements indicated different ion ratios and high amounts of oxygen near the observed surface irregularities. The pathways suggested by Xiao et al.[37] therefore, cannot be
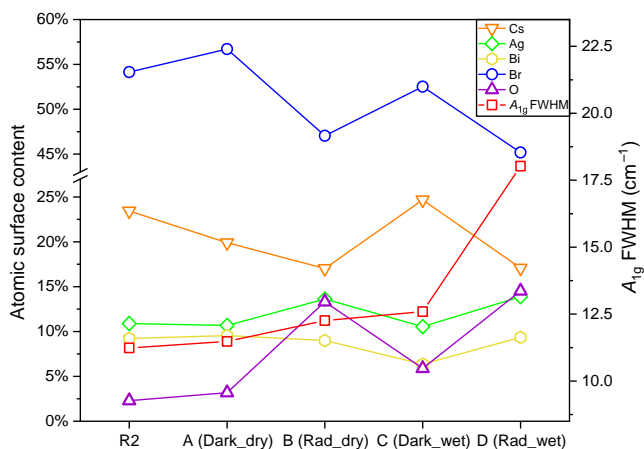
Figure 7. Raman A_{1g} broadening (FWHM, red) and averaged atomic surface content of Ag, Br, and O determined by EDX spectroscopy. Similarities of surface composition trends of both irradiated samples are highlighted.

applied for dry irradiated samples, hinting toward photo-accelerated oxidation behavior. The relation between the high surface oxygen of Samples B and D determined by EDX (Figure 7) and their absorbance increase below bandgap (Figure 2) indirectly reveal oxygen and photoinduced irregularities and defects. Hence, the presence of oxygen in combination with solar radiation accelerated the chemical reaction and resulted in compositional changes for both Samples B and D.

4.5. Surface Sensitivity of Employed Characterization Methods

The most surface-sensitive employed characterization method was Raman analysis, which clearly showed that wet samples obtained high shares of $Cs_3Bi_2Br_9$, indicating a partial chemical phase transformation. Furthermore, the A_{1g} FWHM Raman broadening increased from B to C to D (compare Figure 7). This makes the presence of moisture the major observed cause for severe degradation in $Cs_2AgBiBr_6$. The change in PL properties for the irregularities observed on Sample B compared to R2 hinted toward only insignificant alterations in surface absorption behavior for a sample exposed to radiation and humidity. EDX, known to have higher penetration depth than for instance, Raman, yields significant alterations in averaged surface compositions for wet Samples B and D when compared to Samples A and R2. However, the second highest deviation from the reference R2 (after Sample D: Rad_wet) was observed for Sample B. It is also noteworthy how close the averaged surface contents of Ag, Br, and O were in both radiated Samples B and D (Figure 7). As bulk-sensitive characterization method, UV–vis absorption behavior also demonstrated a strong influence of photodegradation. The irradiated samples (B and D) obtained the highest absorption below the bandgap, which indicated photoinduced lattice defect formations in both illuminated samples (Figure 2). Interestingly, Sample B yielded the high absorption behavior at around 450 nm, which could be a hint for the presence of $Cs_3Bi_2Br_9$ with its comparably high bandgap of around 2.6 eV.[31,33] However, no secondary phases could be found.

XRD patterns in Figure S5, Supporting Information, were obtained by grinding the samples. XRD is therefore the most bulk-sensitive characterization method included in this study. Overall, moisture-induced degradation was most obvious when analyzing data obtained via Raman spectroscopy, while no clear sign for photodegradation was visible in the Raman spectrum of Sample B. However, the more bulk-sensitive methods EDX and UV–vis spectroscopy found clear correlations between the degeneration of both irradiated samples (B: Rad_dry and D: Rad_wet), indicating chemical alterations as well as defects of $Cs_2AgBiBr_6$. The observed ion migration was found to be accelerated in the presence of simulated sunlight, hinting toward the fact that the energy barriers for the migration might be easier to overcome in the presence of water combined with sunlight.[37] This should be further investigated for the long-term performance enhancement of $Cs_2AgBiBr_6$-based PSCs in ambient conditions. Furthermore, oxidation occurred on the irradiated samples as higher oxygen content was observed by EDX spectroscopy. From these observations, it was concluded that the presence of water primarily influences the chemical compositional change on the surface of samples. The simulated AM1.5g light exposure induced and accelerated degradation processes resulting in lattice defects and surface irregularities in $Cs_2AgBiBr_6$.

4.6. Regenerative Synthesis

Even though recycled HBr solvent showed visible darkening after the second synthesis (Figure S6, Supporting Information), the regenerative synthesis of sample RS resulted in a relative yield compared to the reference R4 (see Table 5). No secondary phases could be observed through Raman analysis (Figure 5b,c). Furthermore, the A_{1g} FWHM value of 11.25 cm^{-1} (compared to 11.14 cm^{-1} for R4) and a similar bandgap value (Table 5) indicated a successful regenerative synthesis. Hence, it can be concluded that intact $Cs_2AgBiBr_6$ single crystals were synthesized from the used HBr solvent. The high absorption background (Figure 5a) and darkening of the solvent and crystal surfaces likely originated from carbon impurities from using organic filter paper during the previous sampling. We recommend utilizing nonreactive extraction methods like glass filters for single crystals or other film deposition techniques that aim toward regenerative synthesis at a larger scale. Furthermore, during the preparation of preused HBr solvent, its remaining precursor concentration was estimated by simply considering the previous crystal yield. It turned out that the precursor concentration was overestimated because precursor leftovers in the filter paper could not be correctly measured. Therefore, adopting a higher precursor concentration than estimated from previous yields should be considered when aiming to further increase the yield of regenerative $Cs_2AgBiBr_6$ synthesis methods.

5. Conclusion

$Cs_2AgBiBr_6$ single crystals demonstrated heavy alterations and chemical changes after the exposure to aquatic conditions. The degradation process was accelerated by simulated solar irradiation resulting in surface irregularities and photoinduced

defects. In both wet samples, the formation of multiple secondary phases was confirmed. The $Cs_2AgBiBr_6$ reference did not exhibit any sign of degradation or property change for 2 months, meaning there was no spontaneous decomposition detected, proving intrinsic time stability. $Cs_2AgBiBr_6$ single crystals are inherently stable, and the material can be recommended for multi-junction photovoltaics due to their suitable bandgap. However, through the results of this study, it became obvious that there is further need for research regarding the sealing of $Cs_2AgBiBr_6$ layers when employed in PSCs to protect the structure against humidity and water intrusion. Other possible solutions to increase the stability and efficiency of halide perovskites are the introduction of interface passivation, e.g., via low-dimensional perovskite passivators in PSC design, or approaches like including additives during crystal synthesis or varying precursor composition.[26,42–44] Furthermore, a high potential yield could be obtained from the regenerative synthesis of lead-free $Cs_2AgBiBr_6$ single crystals. These findings may pave the way toward sustainably scaling the production of $Cs_2AgBiBr_6$ while simultaneously saving solvent and therefore having a positive impact toward cost reduction and resource efficiency.

The main findings of this study can be summarized as follows: proven stability of $Cs_2AgBiBr_6$ single crystals after >60 d without significant absorption loss or structural change; observed instability toward moisture with signs of the formation of $Cs_3Bi_2Br_9$, $CsAgBr_2$, $CsBr$, and $BiBrO$; photoinduced degradation resulting in discolorations, surface irregularities, and lattice defects after AM1.5g solar simulation for 140 h; and great potential for regenerative synthesis by solvent recycling for $Cs_2AgBiBr_6$ synthesis with promising properties and high relative yield.

Supporting Information

Supporting Information is available from the Wiley Online Library or from the author.

Conflict of Interest

The authors declare no conflict of interest.

Data Availability Statement

The data that support the findings of this study are available from the corresponding author upon reasonable request.

Keywords

$Cs_2AgBiBr_6$, lead-free photovoltaics, perovskite solar cells, stability studies

[1] Best Research-Cell Efficiency Chart, https://www.nrel.gov/pv/assets/pdfs/cell-pv-eff-emergingpv.pdf (accessed: September 2023).

[2] J. Liang, X. Hu, C. Wang, C. Liang, C. Chen, M. Xiao, J. Li, C. Tao, G. Xing, R. Yu, W. Ke, G. Fang, *Joule* **2022**, *6*, 816.

[3] C. Wu, Q. Zhang, Y. Liu, W. Luo, X. Guo, Z. Huang, H. Ting, W. Sun, X. Zhong, S. Wei, S. Wang, Z. Chen, L. Xiao, *Adv. Sci.* **2018**, *5*, 1700759.

[4] A. H. Slavney, T. Hu, A. M. Lindenberg, H. I. Karunadasa, *J. Am. Chem. Soc.* **2016**, *138*, 2138.

[5] X. Yang, W. Wang, R. Ran, W. Zhou, Z. Shao, *Energy Fuels* **2020**, *34*, 10513.

[6] P. Schygulla, R. Müller, D. Lackner, O. Höhn, H. Hauser, B. Bläsi, F. Predan, J. Benick, M. Hermle, S. W. Glunz, F. Dimroth, *Prog. Photovoltaics Res. Appl.* **2021**, *30*, 869.

[7] J. Zeitouny, E. A. Katz, A. Dollet, A. Vossier, *Sci. Rep.* **2017**, *7*, 1766.

[8] Z. Zhang, Q. Sun, Y. Lu, F. Lu, X. Mu, S.-H. Wei, M. Sui, *Nat. Commun.* **2022**, *13*, 3397.

[9] Y. Ou, Z. Lu, J. Lu, X. Zhong, P. Chen, L. Zhou, T. Chen, *Opt. Mater.* **2022**, *129*, 112452.

[10] M. T. Islam, M. R. Jani, S. M. Al Amin, M. S. U. Sami, K. M. Shorowordi, M. I. Hossain, M. Devgun, S. Chowdhury, S. Banerje, S. Ahmed, *Opt. Mater.* **2020**, *105*, 109957.

[11] W. Gao, C. Ran, J. Xi, B. Jiao, W. Zhang, M. Wu, X. Hou, Z. Wu, *Chemphyschem* **2018**, *19*, 1696.

[12] Y. Hu, L. Song, Y. Chen, W. Huang, *Sol. RRL* **2019**, *3*, 1900080.

[13] C. N. Savory, A. Walsh, D. O. Scanlon, *ACS Energy Lett.* **2016**, *1*, 949.

[14] A. C. Dakshinamurthy, C. Sudakar, *Mater. Adv.* **2022**, *3*, 5813.

[15] M. Ghasemi, L. Zhang, J.-H. Yun, M. Hao, D. He, P. Chen, Y. Bai, T. Lin, M. Xiao, A. Du, M. Lyu, L. Wang, *Adv. Funct. Mater.* **2020**, *30*, 2002342.

[16] K. P. Lindquist, S. A. Mack, A. H. Slavney, L. Leppert, A. Gold-Parker, J. F. Stebbins, A. Salleo, M. F. Toney, J. B. Neaton, H. I. Karunadasa, *Chem. Sci.* **2019**, *10*, 10620.

[17] W. Ning, X.-G. Zhao, J. Klarbring, S. Bai, F. Ji, F. Wang, S. I. Simak, Y. Tao, X.-M. Ren, L. Zhang, W. Huang, I. A. Abrikosov, F. Gao, *Adv. Funct. Mater.* **2019**, *29*, 1807375.

[18] X.-F. Cheng, W.-H. Qian, J. Wang, C. Yu, J.-H. He, H. Li, Q.-F. Xu, D.-Y. Chen, N.-J. Li, J.-M. Lu, *Small* **2019**, *15*, 1905731.

[19] P. Pistor, M. Meyns, M. Guc, H.-C. Wang, M. A. Marques, X. Alcobé, A. Cabot, V. Izquierdo-Roca, *Scr. Mater.* **2020**, *184*, 24.

[20] Y. Zhang, T. Shah, F. L. Deepak, B. A. Korgel, *Chem. Mater.* **2019**, *31*, 7962.

[21] E. Greul, M. L. Petrus, A. Binek, P. Docampo, T. Bein, *J. Mater. Chem. A* **2017**, *5*, 19972.

[22] M. Shi, G. Li, W. Tian, S. Jin, X. Tao, Y. Jiang, E. A. Pidko, R. Li, C. Li, *Adv. Mater.* **2020**, *32*, 2002137.

[23] M. Wang, W. Wang, B. Ma, W. Shen, L. Liu, K. Cao, S. Chen, W. Huang, *Nano-Micro Lett.* **2021**, *13*, 62.

[24] H. Lei, D. Hardy, F. Gao, *Adv. Funct. Mater.* **2021**, *31*, 2105898.

[25] L. Yin, H. Wu, W. Pan, B. Yang, P. Li, J. Luo, G. Niu, J. Tang, *Adv. Opt. Mater.* **2019**, *7*, 1900491.

[26] A. Frebel, S. Yoon, S. Meles Neguse, D. M. Jöckel, M. Widenmeyer, S. Lange, V. Naumann, A. Rosspeintner, S. G. Ebbinghaus, B. Balke, A. Weidenkaff, *Adv. Photonics Res.* **2022**, *3*, 2200061.

[27] P. Kubelka, F. Munk, *Z. Tech. Phys.* **1931**, *12*, 593.

[28] P. Makuła, M. Pacia, W. Macyk, *J. Phys. Chem. Lett.* **2018**, *9*, 6814.

[29] S. J. Zelewski, J. M. Urban, A. Surrente, D. K. Maude, A. Kuc, L. Schade, R. D. Johnson, M. Dollmann, P. K. Nayak, H. J. Snaith, P. Radaelli, R. Kudrawiec, R. J. Nicholas, P. Plochocka, M. Baranowski, *J. Mater. Chem. C* **2019**, *7*, 8350.

[30] S. Bonomi, P. Galinetto, M. Patrini, L. Romani, L. Malavasi, *Inorg. Chem.* **2021**, *60*, 14142.

[31] M. Roy, S. Ghorui, Bhawna, J. Kangsabanik, R. Yadav, A. Alam, M. Aslam, *J. Phys. Chem. C* **2020**, *124*, 19484.

[32] S. Yoon, B. Fett, A. Frebel, S. Kroisl, B. Herbig, M. Widenmeyer, B. Balke, G. Sextl, K. Mandel, A. Weidenkaff, *Energy Technol.* **2022**, *10*, 2200197.

[33] Y. Dai, H. Tüysüz, *Sol. RRL* **2021**, *5*, 2100265.

[34] E. T. McClure, M. R. Ball, W. Windl, P. M. Woodward, *Chem. Mater.* **2016**, *28*, 1348.

[35] B.-B. Yu, M. Liao, J. Yang, W. Chen, Y. Zhu, X. Zhang, T. Duan, W. Yao, S.-H. Wei, Z. He, *J. Mater. Chem. A* **2019**, *7*, 8818.

[36] C. Tomasi, F. Tampieri, *Atmos. Environ.* **1976**, *10*, 1005.

[37] Z. Xiao, W. Meng, J. Wang, Y. Yan, *ChemSusChem* **2016**, *9*, 2628.

[38] N. H. Makani, M. Singh, T. Paul, A. Sahoo, J. Nama, S. Sharma, R. Banerjee, *J. Electroanal. Chem.* **2022**, *920*, 116583.

[39] P. Fan, H.-X. Peng, Z.-H. Zheng, Z.-H. Chen, S.-J. Tan, X.-Y. Chen, Y.-D. Luo, Z.-H. Su, J.-T. Luo, G.-X. Liang, *Nanomaterials* **2019**, *9*, 1760.

[40] N. Haram, N. Ahmad, *J. Clust. Sci.* **2015**, *26*, 713.

[41] A. Band, A. Albu-Yaron, T. Livneh, H. Cohen, Y. Feldman, L. Shimon, R. Popovitz-Biro, V. Lyahovitskaya, R. Tenne, *J. Phys. Chem. B* **2004**, *108*, 12360.

[42] X. Yang, H. Xiang, J. Huang, C. Zhou, R. Ran, W. Wang, W. Zhou, Z. Shao, *J. Colloid Interface Sci.* **2022**, *628*, 476.

[43] W. Shen, Y. Dong, F. Huang, Y.-B. Cheng, J. Zhong, *Mater. Rep. Energy* **2021**, *1*, 100060.

[44] Y. Zhao, H. Xiang, R. Ran, W. Zhou, W. Wang, Z. Shao, *J. Energy Chem.* **2023**, *83*, 189.